# Nanoscale

Accepted Manuscript


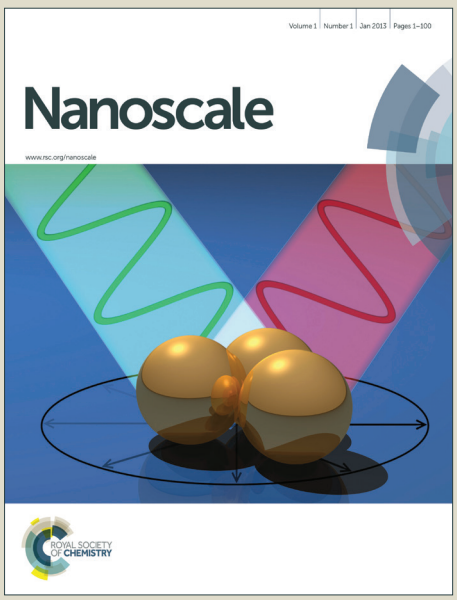





ROYAL SOCIETY OF CHEMISTRY

www.rsc.org/nanoscale

Nanoscale

PAPER

# Importance of polypyrrole in constructing 3D hierarchical carbon nanotube@$MnO_2$ perfect core-shell nanostructures for high-performance flexible supercapacitors

Received 00th January 20xx,
Accepted 00th January 20xx

DOI: 10.1039/x0xx00000x

www.rsc.org/

Jinyuan Zhou, ‡* Hao Zhao,‡ Xuemei Mu, Jiayi Chen, Peng Zhang, Yaling Wang, Yongmin He, Zhenxing Zhang, Xiaojun Pan and Erqing Xie*

This study reports the preparation of 3D hierarchical carbon nanotube (CNT) @$MnO_2$ core-shell nanostructures under assistance of polypyrrole (PPy). The as-prepared CNT@PPy@$MnO_2$ core-shell structures show a perfect coating of $MnO_2$ on each CNT and, more importantly, a robust bush-like pseudocapacitive shell to effectively increase the specific surface area and enhance the ion accessibility. As expected, a high specific capacity of 490-530 F $g^{-1}$ has been achieved from CNT@PPy@$MnO_2$ single electrode. And about 98.5% of the capacity is retained after 1000 charge/discharge cycles at current density of 5 A $g^{-1}$. Furthermore, the assembled asymmetric CNT@PPy@$MnO_2$//AC capacitors show the maximum energy density of 38.42 W h $kg^{-1}$ (2.24 mW h $cm^{-3}$) at power density of 100 W $kg^{-1}$ (5.83 mW $cm^{-3}$), and maintain 59.52% of the initial value at 10,000 W $kg^{-1}$ (0.583 W $cm^{-3}$). In addition, the assembled devices show high cycle stabilities (89.7% after 2000 cycles for asymmetric, and 87.2% for symmetric), and high bending stability (64.74% after 200 bending tests). This ability to obtain high energy density at high power rates while maintaining high cycle stability demonstrates that this well-designed structure could be a promising electrode material for high-performance supercapacitors.

## Introduction

Recently, supercapacitors (also called electrochemical capacitors) have attracted intensive attention due to their high power densities and high cycle stabilities.[1, 2] However, those supercapacitors possess a fatal flaw, i.e., low energy density, which greatly hindered their further development and applications compared to the commercial batteries.[3, 4] To obtain a high energy density, various pseudocapacitive materials have incorporated into the electrodes for supercapacitors due to their high specific capacitance resulting from stable redox reactions.[5-7] As a pseudocapacitive material, $MnO_2$ show many advantages such as high abundance, low cost, chemical stability, and high theoretical specific capacitance of 1370 F $g^{-1}$.[8] Like most pseudocapacitive materials, unfortunately, $MnO_2$ possesses a very low electrical conductivity ($10^{-5}$~$10^{-6}$ S $cm^{-1}$)[9, 10], greatly limiting the charge transfer during the charge/discharge process and accordingly decreasing energy density of their counterpart supercapacitors.

To overcome the above problem, many hierarchical carbon nanostructures have been applied to improving their energy density.[11-14] These nanostructures can not only work as charge-transfer highways, but also increase the special surface area of the electrodes and shorten the diffusion distance of the ions. In particular, carbon nanotubes (CNTs) have frequently used as conductive additives in electrode materials.[15-20] As for the design of hierarchical CNT-$MnO_2$ composites, it is an ideal idea that pseudocapacitive materials can be uniformly coated on the surface of CNTs to obtain a large ionic reaction interface and a short ion diffusion distance. However, due to their super chemical properties, it is demonstrated hard to uniformly coat $MnO_2$ on the surface of an individual CNT, just forming CNT-$MnO_2$-particle composites.[21, 22] And this situation often greatly limits the improvement in charge transport performances of supercapacitors. Then, various pre-treatments, such as acid, alkali or electrochemical treatments, have been applied to generating more oxygen function groups on the surface of CNTs that are helpful to the absorption of $MnO_2$ nanoparticles.[23] More often, those oxygen function groups first form at CNTs' defect sites that are random and non-uniform, and usually induce the formation of $MnO_2$ clusters, even bulk $MnO_2$.[24, 25] Thus, it is still urgent and important to further explore the design and fabrication of a type of high-efficient charge-transfer highways of CNT@$MnO_2$ core shell structures. More recently, Li et al.[26] have reported a type of CNT@polypyrrole (PPy) @$MnO_2$ core-double-shell structures and obtained highly improved electrochemical performances.

Herein, we have designed and fabricated a type of 3D hierarchical CNT@$MnO_2$ perfect core-shell nanostructures by introducing a conductive polymer (PPy) to modify the surface

* School of Physical Science and Technology, Lanzhou University, Lanzhou, Gansu, 730000, People's Republic of China. E-mail: zhoujy@lzu.edu.cn, xieeq@lzu.edu.cn; Tel/fax: +86 931 89125895
†Electronic Supplementary Information (ESI) available: See
DOI: 10.1039/x0xx00000x
‡ These authors contributed equally to this work.

of hierarchical CNTs before $MnO_2$ loading. Results showed that the obtained 3D hierarchical CNT@PPy@$MnO_2$ possess a uniform core-shell structure of CNT@$MnO_2$, indicating the importance of PPy for coating $MnO_2$ on CNTs. Moreover, series of electrochemical characterizations showed that the specific capacitance, rate capabilities, and capacitance retention of CNT@PPy@$MnO_2$ electrodes are rather superior to those of CNT@$MnO_2$ electrodes. These enhancements are mainly due to three aspects: 1) the greatly improved the adhesion between $MnO_2$ and CNTs, leading to high cycle stability of the electrodes; 2) to construct perfect core-shell structure of CNT@PPy@$MnO_2$, decreasing the electrolyte contact resistance of the electrodes; and 3) the formed 3D hierarchical $MnO_2$ nanosheets possess a much high specific surface, largely increasing the specific capacitance of the electrodes. Furthermore, the assembled asymmetric supercapacitor based on CNT@PPy@$MnO_2$ electrodes demonstrates the maximum energy density of 38.42 W h $kg^{-1}$ and a high retention rate of 59.53% even at the power density up to 10,000 W $kg^{-1}$. In addition, the asymmetric supercapacitors also exhibit high cycling and bending stabilities.

## Experimental

### Growth of CNTs on SSMs

CNTs were grown by a thermal CVD technique,[27] and a type of commercial 316# stainless steel meshes (SSMs) with size of 1 cm × 2 cm was chosen as substrates. Before CNT growth, the well-washed SSMs were immersed in iron acetylacetonate/ ethanol solution with a concentration of 5 mM for a 10-min catalyst coating. After dried for 1 min, the SSMs were then placed in a one-inch quartz-tube furnace. And the CNT growth procedure is as follows: First, the furnace was quickly heated up to 700 °C for 20 min in ambient air, then a mixture flow of Ar (150 sccm) and $H_2$ (50 sccm) was introduced into the quartz tube, and the furnace was further heated up to 750 °C and kept for 15 min. After hydrogen reduction treatments, another flow of acetylene ($C_2H_2$) was added into the Ar/$H_2$ stream (Ar of 200 sccm, $H_2$ of 20 sccm, $C_2H_2$ of 30 sccm) to start the CNT growth at 750 °C, and the growth process was kept for 60 min. Finally, the furnace was quickly cooled down to the temperature lower than 50 °C before taking out the samples for analysis and deposition of PPy and $MnO_2$.

### Fabrication of CNT@PPy@$MnO_2$ core-shell structures.

### PPy treatment to CNTs

To enhance the $MnO_2$ coating on CNTs, PPy treatments have been done to the CNTs grown on SSMs by an electropolymerization technique.[28] Prior to the PPy treatments, hydrophilic treatments have been applied to the grown CNTs by a electrochemical approach, in which 1 M $Na_2SO_4$ was used as electrolyte and galvanostatic charge-discharge (GCD) processes were conducted at 2.5 mA $cm^{-2}$ (0 ~ 0.8 V) for 10 cycles. Then, the treated and well-washed CNTs were taken to another electrochemical process for further PPy treatments. In this process, a solution of 0.2 M $NaClO_4$ containing 5% (V:V) pyrrole monomer was used as electrolyte, and a constant voltage of 0.92 V was applied, and the electropolymerization process was maintained for 5, 10, 20, 40, 60, and 120 seconds. Both electrochemical treatments above were conducted in a three-electrode system on an electrochemical workstation (CS350, Wuhan Corrtest Instruments Co., Ltd., China) under ambient conditions, in which here and thereafter a Ag/AgCl electrode is used as reference electrode, a platinum foil as counter electrode, and the samples as working electrode.

### $MnO_2$ deposition on CNTs

The $MnO_2$ deposition was conducted in a hydrothermal process. First, 0.03 M $KMnO_4$ solution was prepared and transferred into a Teflon-lined stainless steel autoclave. After loading the samples (PPy-treated or untreated), the autoclave was then sealed and maintained at 60 °C for 0.5, 1, 3, 5, and 7 h. Finally, the resulting mesh was rinsed with DI water and naturally dried at room temperature.

### Electrochemical tests

All electrochemical tests were carried out at room temperature. In single-electrode tests, a three-electrode system was used to measure the CV with potential ranging from 0 to 1 V at different scan rates, galvanostatic charge/discharge (GCD) behaviours with potential ranging from 0 to 1 V at different current densities, and electrochemical impedance spectroscopy (EIS) in the frequency range from 0.1 to $10^5$ Hz at the open-circuit voltage with an alternating amplitude of 5mV.

In full-cell tests, a two-electrode system was used. for the asymmetric supercapacitor, a piece of SSM/CNT@PPy@$MnO_2$ (1 cm × 2 cm, 0.15 mg of PPy and 0.55 mg of $MnO_2$) and a piece of SSM/activated carbon (AC) (1 cm × 2 cm, 1.75 mg of AC) were separated by a ~30-μm-thick polymer membrane (DR2012, Suzhou Beige New Materials & Technology Co. Ltd.) and used as positive and negative electrode, respectively. Two copper tapes were used as lead wires that adhere to each electrode. Then, two piece of polyethylene terephthalate (PET) membrane (thickness of ~40 μm) were used to assemble the two electrodes containing electrolyte (1 M $Na_2SO_4$ aqueous solution) into a sandwich configuration. Finally, the device was sealed with plastic adhesive tape and instant adhesive. It is noted that the SSM/AC composites were prepared by dropping the AC ink (including 85 wt% AC, 10 wt% acetylene black, and 5 wt% polyvinylidene fluoride binder in N-methyl-2-pyrrolidone solvent) on the SSM.

For comparison, a type of symmetric supercapacitors was also assembled with the same configuration with the above asymmetric ones. Two similar pieces of SSM@CNT@PPy@$MnO_2$ (or SSM@CNT@$MnO_2$) were used as the positive and negative electrodes, respectively, and the total thickness and weight of all devices is less than 1 mm and 10 mg, respectively. The CV, GCD and EIS spectra of the assembled devices were performed by respectively connecting their positive and negative electrodes with working and counter electrodes and short-circuiting the reference electrode with the counter electrode. And the other parameters were the same with those of the single-electrode tests.

Calculation: The specific capacitance ($C_s$, F $g^{-1}$) values were calculated from the *C*V data according to the following equations:

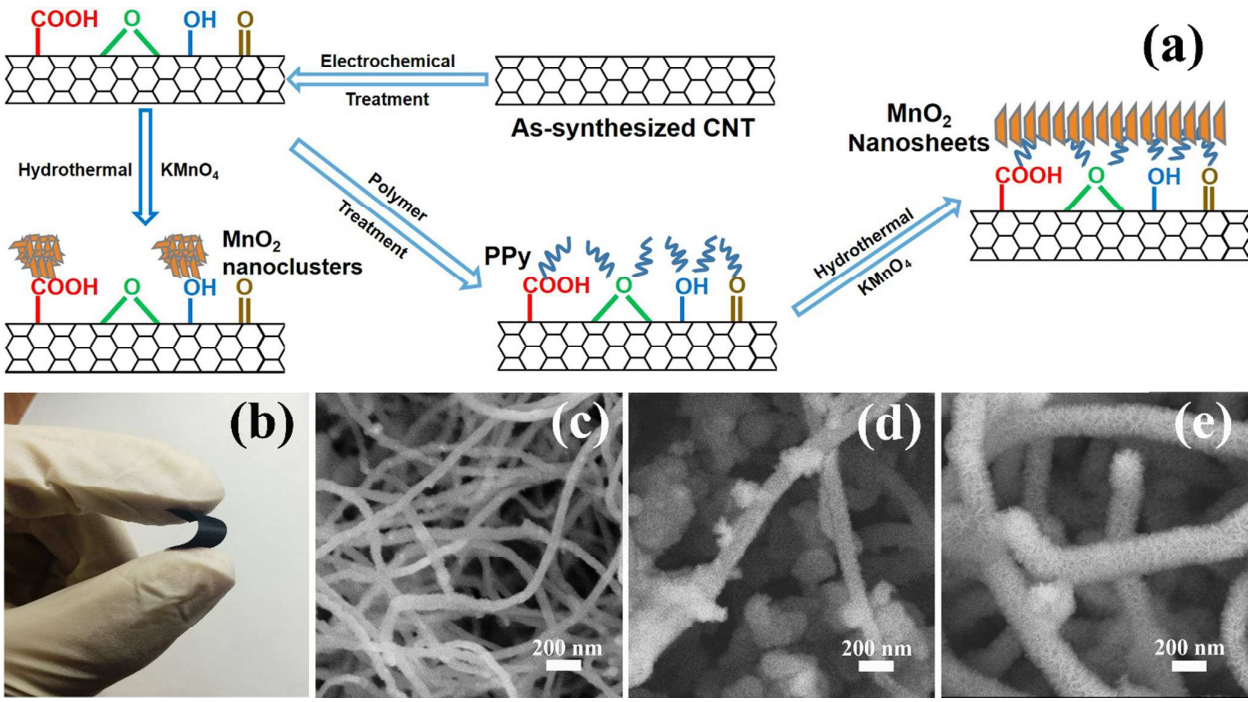


Fig. 1 (a) Schematic illustration for fabrication process of CNT@$MnO_2$ core-shell structures, (b) digital photograph and (c) SEM image shows as-synthesized CNTs by CVD, (d) and (e) SEM images of CNT@$MnO_2$ structures without and with PPy modification, respectively.

$$C_s=(\int I dV)/mv(\Delta U), \quad (1)$$

where $C_s$ is the specific capacitance, $I$ is the response current, $v$ is the potential scan rate (V/s), and $\Delta U$ is the applied potential, $m$ is the mass of active material.

The $C_s$ can also be calculated from the GCD curve based on equation:

$$C_s=(\int I dt)/m(\Delta U) \quad (2)$$

where $t$ is the discharge time.

And the volumetric capacitance ($C_V$) can be calculated by replacing $m$ in Eqs. (1) and (2) with the volume ($V$, $cm^{-3}$). This volume is the whole volume of the device, including the volumes of SSM/CNT @PPy@$MnO_2$ electrodes, the encapsulating PET membranes, and the polymer separator. In our case, the devices are 2 cm in length and 1 cm in width; and the thickness of the components (electrodes, PET membranes, and polymer separator) are measured by an Olympus BX51 microscope. The energy density and power density of the device was obtained from the equations:

$$E= C\times\Delta U^2/7200, \quad (3)$$

$$P=E\times 3600/\Delta t, \quad (4)$$

where $E$ is the energy density (in W h $kg^{-1}$ using $C_s$ or W h $cm^{-3}$ using $C_V$), P is the power density (in W $kg^{-1}$ or W $cm^{-3}$) and $\Delta t$ is the discharge time.

**Material Characterization.**

The morphologies of the obtained structures were characterized by field emission scanning electron microscopy (FE-SEM, Hitachi S-4800) with an accelerating voltage of 5 kV. Their fine structures were characterized using transmission electron microscopy (FEI Tecnai F30, operated at 300 kV). The chemical component was analysed on a micro-Raman spectroscope (JY-HR800, 532-nm wavelength YAG laser) and a multifunctional X-ray photoelectron spectroscope (PHI-5702, Mg KR X-ray, 1253.6 eV). The masses of the deposited $MnO_2$ and PPy were measured by a microbalance (Mettler, XS105DU).

## Results and discussion

**Preparation and characteristics**

Fig. 1(a) schematically illustrates the process in fabricating CNT@$MnO_2$ core-shell structures for electrode materials of supercapacitors. As reported previously, the as-synthesized CNTs (Figs. 1(b) and 1(c)) should be electrochemically treated before $MnO_2$ deposition before a hydrothermal process. Then, the formed limited oxygenated functional groups (such as epoxide, carboxyl, and/or hydroxyl) by electrochemical treatments can enhance the deposition of $MnO_2$ to some extent, and the deposited $MnO_2$ is usually in form of nanoclusters with size of several tens of nanometers, as shown in Fig. 1(d). Unfortunately, it is demonstrated that this type of $MnO_2$ nanoclusters show a relatively low pseudocapacitive behaviour.[29] On the other hand, those oxygenated functional groups can also benefit the deposition of electrically conducting polymers on CNT materials,[30] For instance, one oxygenated functional group can absorb one $MnO_2$ nanoparticle, and it can likewise absorb a polymer chain. While one polymer chain usually contains several to several tens of monomers, each of which can absorb one $MnO_2$ nanoparticles. Thus, the polymer treatment can greatly enhance the $MnO_2$ deposition. In our case, a type of pseudocapacitive polymer,

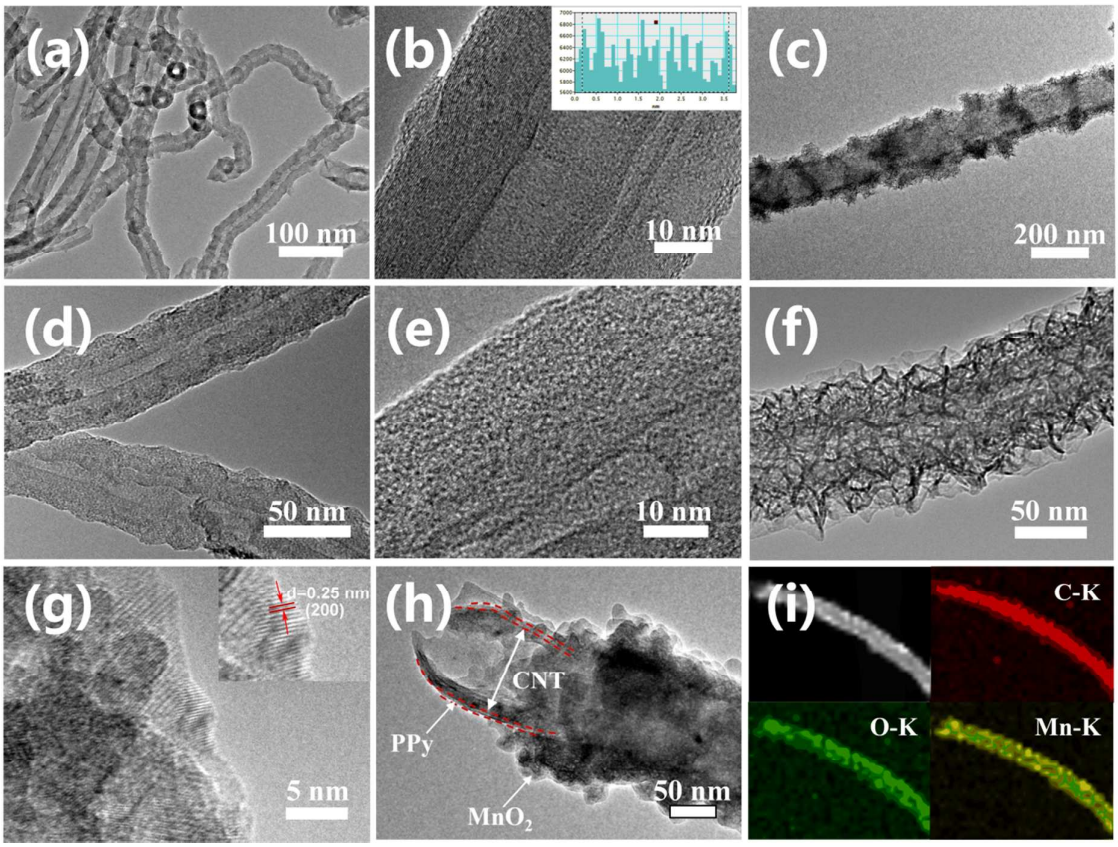


Fig. 2 TEM images of (a) CNTs, (c) CNT@$MnO_2$, (d) CNT@PPy core-shell structures, and (f) CNT@PPy@$MnO_2$ core-shell structures; (b), (e) and (g) the corresponding HRTEMs images of (a), (c), and (f), respectively. The inset in (b) shows the wall spacing of MWCNTs, and the inset in (g) indicates the lattice spacing of <200> crystalline plane of $MnO_2$. (h) high-magnification TEM image shows the core-shell structure; (f) HADDF-STEM image of individual CNT@PPy@$MnO_2$ core-shell structure and the corresponding EDX mapping images of C, O, and Mn elements.

PPy, was used to enhance the $MnO_2$ deposition on CNTs. Under assistance of PPy, the $MnO_2$ deposition on CNTs are greatly enhanced (Fig. 1(e)), in form of nanosheets. Here, it is noted that the critical advantage of this polymer modification of CNT materials is to easily obtaining a perfect CNT@$MnO_2$ core-shell structure. Alternatively, this polymer modification can also be used to design other pseudocapacitive core-shell structures for electrodes. And this approach is both straightforward and cost-effective, and could easily fit into a scalable, roll-to-roll process for industrial production of flexible CNT-based energy storage systems.

Further characterizations of the microstructures of the prepared samples were conducted on a TEM. The grown CNTs have an average diameter of ~40 nm with wall-thickness of about 10 nm (Fig. 2(a)). And the CNT are about 30-walled CNTs with spacing of about 0.34 nm (Fig. 2(b)). Fig. 2(c) shows the deposited $MnO_2$ without PPy modification is not uniformly on the surface of CNTs and in form of nanoclusters, which is consistent with the SEM result above. Fig. 2(d) shows the morphologies of CNT@PPy core-shell structures, in which the PPy shells are about 10 nm and uniform all over the surface of CNTs. Moreover, this type of core-shell structure exhibits a good contact between PPy and CNTs (Fig. 2(e)). Under assistant of PPy, a type of CNT@PPy@$MnO_2$ perfect core-shell structures was obtained, as shown in Fig. 2(f). Interestingly, the loaded $MnO_2$ on CNT@PPy structures are in form of crystalline nanosheets (Fig. 2g), which will result in more accessible surface area and thus better electrochemical performances. Moreover, the inset in Fig. 2g indicates the lattice fringes with spacing of about 0.25 nm, which correspond to the <200> plane of birnessite-type $MnO_2$.[31] To more clearly characterize CNT@PPy@$MnO_2$ core-shell structure, we carefully chose a TEM test at one tip, as marked in Fig. 2(h). The CNT wall, PPy shell and $MnO_2$ coating can be roughly distinguished. More information of core-shell microstructures can be revealed from the chemical element distributions of CNT@PPy@$MnO_2$ core-shell structure by HAADF-STEM and EDX elemental mapping analysis techniques (Fig. 2(i)). The upper left figure in 2(f) shows a representative HADDF-STEM image of core-shell structure. The contrast of incoherent high-resolution HADDF-STEM images depends directly on the sample atomic number and thickness for the materials. It reveals a tubular structure and a uniform chemical composition. The corresponding EDX mappings of C (Kα, 0.26 keV), O (Kα, 0.52 keV), , and Mn (Kα, 5.9 keV) elements show that the elements C is evenly

distributed in the inner shell, O and Mn are evenly throughout the outer shell, indicating a perfect shell structure of $MnO_2$.

Raman spectra have been employed to characterize the chemical components in various samples. As shown in Fig. 3(a), the typical three Raman bands at 1583 (G band), 1353 (D band), and 2693 $cm^{-1}$ (2D band) can be observed from the pristine CNTs.[17, 32, 33] After $MnO_2$ loading (CNT@$MnO_2$), three new Raman bands locating at 502, 576, and 635 $cm^{-1}$ are in good agreement with the three major vibrational features of the birnessite-type $MnO_2$.[34, 35] As for PPy coated CNTs (CNT@PPy), two new peaks appearing at about 912 and 1035 $cm^{-1}$, which correspond to be the symmetric stretching mode of $ClO_4^-$ dopants[36] and the N-H in-plane deformation of PPy[37]. These results are in good agreement with the major feature of the polypyrrole electropolymerized in the solution contain $ClO_4^-$. And, another two weak peaks at 862 and 961 $cm^{-1}$ might be due to the ring deformation associated with dication and radical cation,[38] further confirming the existence of PPy. All these peaks also appear in the spectrum of CNT@PPy@$MnO_2$ and well prove the component of PPy in our core-shell structures. Furthermore, the other two low peaks (1218 and 1415 $cm^{-1}$) from PPy disappear in the spectrum of CNT@PPy@$MnO_2$, which might be assigned to the anti-symmetrical stretching mode of the C-H and C-N.[38] This disappearance should be due to the oxidation reaction during the hydrothermal process in the solution of $KMnO_4$.

Further characterization on chemical components was carried out on a XPS. As shown in Fig. 3(b), the full XPS spectrum from CNT@PPy@$MnO_2$ reveals the signals from Mn, O, N, and C elements. Compared to the spectra from pure CNTs, CNT@PPy, and CNT@$MnO_2$, it can be seen that the C 1s peak at 281 eV could be mainly due to the grown CNTs, the N 1s peak at 397 eV to the deposited PPy, and O 1s at 529 eV and Mn 2p at about 650 eV to the loaded $MnO_2$. [39, 40] These results are well consistent with the above Raman results, indicating the existence of PPy and $MnO_2$.

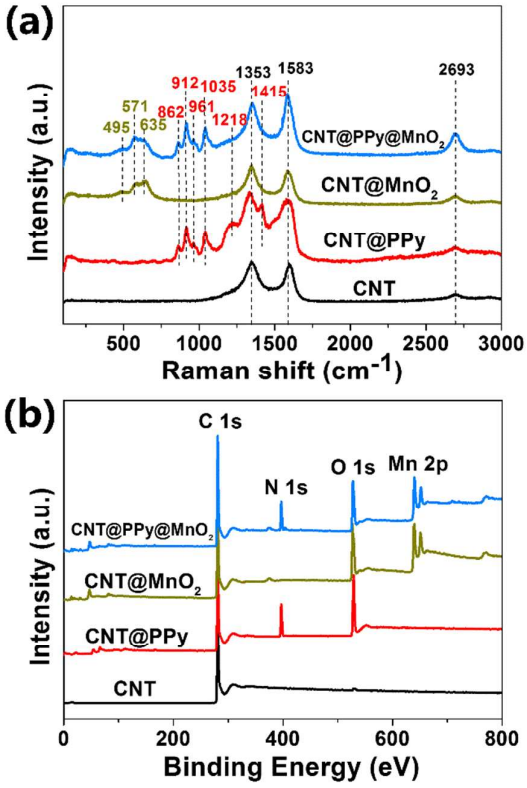


Fig. 3 (a) Raman and (b) XPS spectra of the pristine CNTs, CNT@PPy, CNT@$MnO_2$, and CNT@PPy@$MnO_2$ core-shell structure.

### Electrochemical tests

#### Electrochemical properties of the prepared electrodes

In order to evaluate the electrochemical properties of the CNT@PPy@$MnO_2$ electrodes, the CV curves of CNT@PPy@$MnO_2$ single electrode were first tested at different scan rates. Noted here, to furthest reduce the influence of PPy on the capacitance of the whole electrode, we chose to use the least PPy content in our work. Once the treat time reaches 10 s, the PPy can just cover the CNTs thoroughly, as shown in Figs. S1 and S2. Thus, the deposition mass of PPy in the CNT@PPy@$MnO_2$ electrodes is chosen to be 0.15 mg (0.075 mg $cm^{-2}$). As for the deposition mass of $MnO_2$, as shown in Fig. S3, the optimized deposition time is 3 h and the optimized deposition mass is 0.55 mg (0.275 mg $cm^{-2}$). Thus, in this case, the CNT@PPy@$MnO_2$ electrodes containing 0.15 mg of PPy and 0.55 mg of $MnO_2$ were chosen to conducted series of electrochemical tests.

As shown in Fig. 4(a), the CVs show a quasi-rectangular shape, and almost show no change in curve shape at different scan rates. To investigate the effect of PPy on CV performances of the prepared electrodes, a type of CNT@$MnO_2$ electrodes with $MnO_2$ loading mass of 0.55 mg was also studied for comparison. From Fig. 4(b), it can be seen that the CVs from CNT@$MnO_2$ also show a flat-rectangular shape, and exhibit an obvious current polarization near the potential of 1V. And, it can be seen that the areas covered by

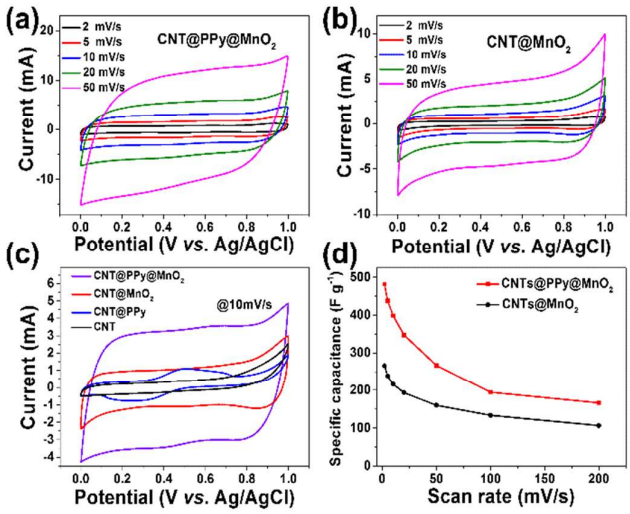


Fig. 4 CV curves of (a) CNT@PPy@$MnO_2$ and (b) CNT@$MnO_2$ at different scan rates; (c) comparison of CV curves from CNTs, CNT@PPy, CNT@$MnO_2$, and CNT@PPy@$MnO_2$ at scan rate of 10 mV $s^{-1}$; (d) specific capacitances of CNT@PPy@$MnO_2$ and CNT@$MnO_2$ as a function of scan rates.

these CVs are much less than those by CNT@PPy@$MnO_2$ electrodes. More comparisons were conducted between four types of electrodes, i.e., CNTs, CNT@$MnO_2$, CNT@PPy, and CNT@PPy@$MnO_2$. As shown in Fig. 4(c), the capacitance from pure CNTs grown on SSMs is very low. After coated a thin layer of PPy, the capacitance from CNT@PPy show a little increase compared to that from CNTs. Comparison between the electrodes with and without $MnO_2$ loading indicates that most capacitance from CNT@$MnO_2$ and CNT@PPy@$MnO_2$ origins from $MnO_2$, and CNTs and PPy can only contribute a small part of capacitance, about 3.3%. Moreover, it can also found that the capacitance of CNT@PPy@$MnO_2$ is much higher than that of CNT@$MnO_2$. The capacitance More details can be reviewed from Fig. 4(d). The specific capacitance of CNT@PPy@$MnO_2$ reaches 481.7 F $g^{-1}$ at scan rate of 2 mV $s^{-1}$, while that of CNT@$MnO_2$ is only 265.8 F $g^{-1}$. Further increasing scan rate up to 200 mV $s^{-1}$, the CNT@PPy@$MnO_2$ electrodes still show a specific capacitance of 181 F $g^{-1}$, and the CNT @$MnO_2$ ones only show a specific capacitance of 106.4 F $g^{-1}$.

To investigate the abilities of delivering energy of the prepared electrodes, the GCD curves of CNT@PPy@$MnO_2$ and CNT@$MnO_2$ electrodes were tested at different charge/discharge currents. Figs. 5(a) and 5(b) compare their GCD curves at different current density (0.1, 0.2, 0.5, 1, 2, 5, and 10 A $g^{-1}$). The GCD curves from both types of electrodes are almost symmetrical for charge and discharge process, and the area covered by the GCD curve from CNT@PPy@$MnO_2$ electrodes is almost double that from CNT@$MnO_2$ ones. More details can be found from Fig 5(c). At 1 A $g^{-1}$, the discharge time of CNT@PPy@$MnO_2$ electrodes is about 400 s, while that of CNT@$MnO_2$ ones is only about 150 s. This comparison in discharge time indicate that the CNT@PPy@$MnO_2$ electrodes have much higher capacitance that CNT@$MnO_2$ ones. Here, using these above series of GCD curves, we calculated the specific capacitances of CNT@PPy@$MnO_2$ and CNT/$MnO_2$ composite electrodes at different current densities; more details can be found in the ESI. As shown in Fig 5(d), the initial specific capacitances at 0.1 A $g^{-1}$ are achieved to be 529.3 and 293.4 F $g^{-1}$ for CNT@PPy@$MnO_2$ and CNT@$MnO_2$ electrodes, respectively. Increasing current density to 10 A $g^{-1}$, the CNT@PPy@$MnO_2$ electrodes still remain a specific capacitance of 303 F $g^{-1}$; while the CNT@$MnO_2$ ones only of 158.7 F $g^{-1}$.

Fig. 5(e) presents the EIS curves of two types of electrodes in the frequency range between 0.01 and 100 kHz. Both EIS curves show a linear shape. The impedance curve of CNT@PPy@$MnO_2$ electrodes shows an inclination angle of about 60°; while that of CNT@$MnO_2$ ones about 35°. Bigger inclination angle usually implies higher capacitive type behaviours, suggesting that the capacitance of CNT@PPy@$MnO_2$ electrodes is higher than that of CNT@$MnO_2$ electrodes. As for the high frequency region, it is mainly associated with two resistances: (1) the solution or electrolyte contact resistance ($R_e$), and (2) the charge transfer resistance ($R_{ct}$).[41] In this case, the EIS curve only intercepts the Z´ axis at $R_e$. It can be seen from the inset figure of Fig. 5(e) that the coating of $MnO_2$ largely increases the $R_e$ of the corresponding electrodes from 1.25 to 3.2 Ω; while the incorporation of PPy into the electrodes only slightly decreases the $R_e$ from 3.2 to 2.8 Ω. Thus, it could be deduced here that the enhanced electrochemical performances are mainly due to the well-designed CNT@$MnO_2$ charge transfer highway and the enhanced accessibility of the ions from the obtained $MnO_2$ nanosheets.

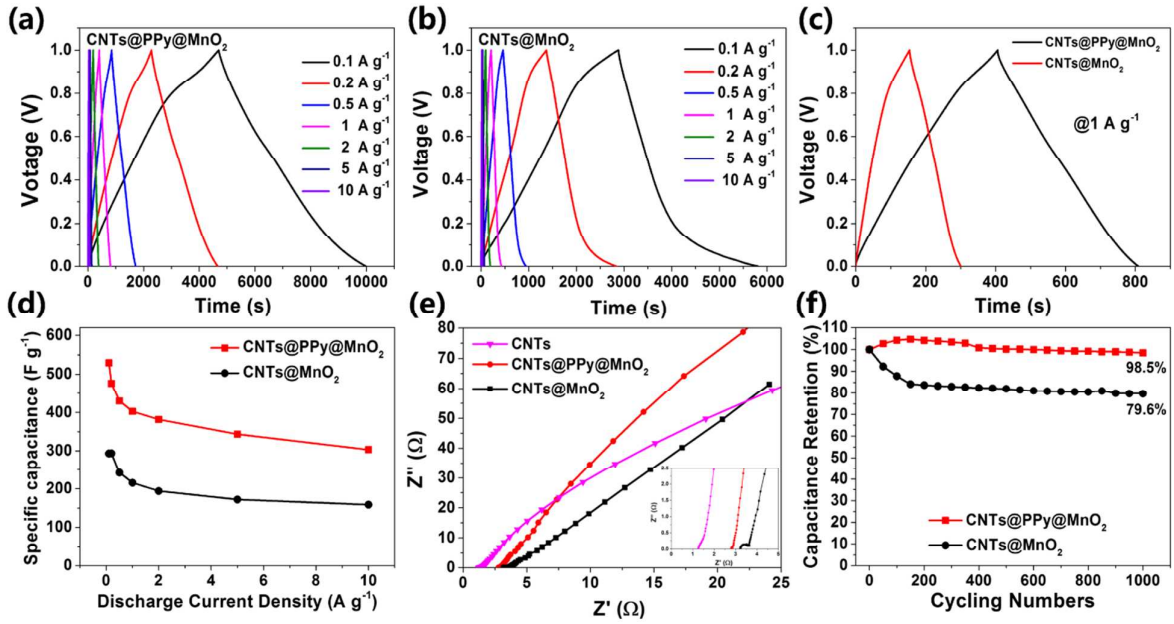


Fig. 5 GCD curves of (a) CNT@PPy@$MnO_2$ and (b) CNT@$MnO_2$ at different discharge current densities; (c) comparison of GCD curves from CNT@PPy@$MnO_2$ and CNT@$MnO_2$ electrodes at current density of 1 A $g^{-1}$; (d) specific capacitance of CNT@PPy@$MnO_2$ and CNT@$MnO_2$ as a function of discharge current densities; (e) Nyquist plots of CNT, CNT@$MnO_2$ and CNT@PPy@$MnO_2$ electrodes, inset: the details of high frequency region; (f) cycling performances of CNT@PPy@$MnO_2$ and CNT@$MnO_2$ electrodes for charge/discharge at current density of 5 A $g^{-1}$.

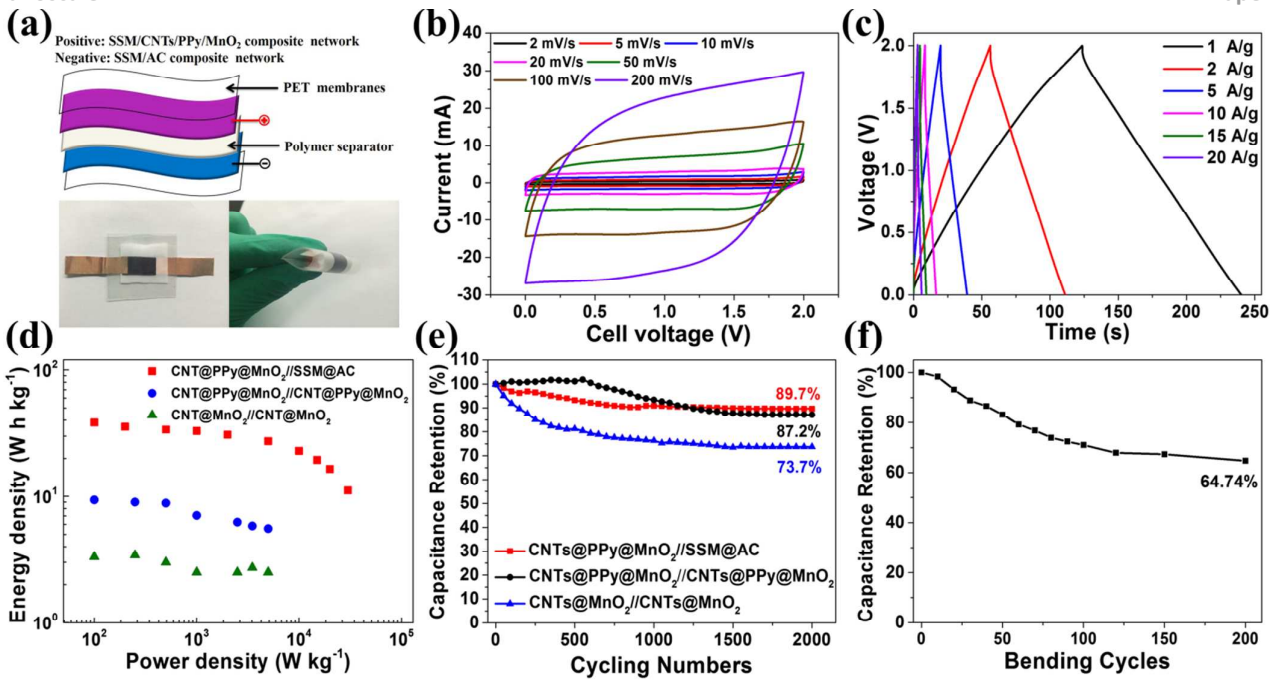


Fig. 6 (a) Schematic illustration of the assembly configuration of our flexible asymmetric supercapacitor, and the two digital photographs at the bottom show the flexible supercapacitor under flat and bending conditions; (b) CVs of the optimized asymmetric supercapacitor at different scan rates, (c) GCDs of the optimized asymmetric supercapacitor at different current densities; (d) Regone plots of the optimized asymmetric supercapacitor and two symmetric supercapacitors; (e) capacitance retention of the optimized asymmetric supercapacitor and two symmetric supercapacitors; and (f) bending cycling performance of the flexible asymmetric supercapacitor at scan rate at 50 mV $s^{-1}$.

In addition, cycling stabilities of CNT@PPy@$MnO_2$ and CNT@$MnO_2$ electrodes have been further investigated at charge/discharge current density of 5 A $g^{-1}$ for 1000 cycles. As shown in Fig. 5(f), the CNT@PPy@$MnO_2$ electrodes show a capacitance retention of about 98.5 %, which is much higher than that of CNT@$MnO_2$ ones (79.6 %). It is noted that the initial slight increase in capacitance retention of CNT@PPy@$MnO_2$ electrodes could be due to the contribution from PPy.

**Electrochemical properties of the assembled supercapacitors**

To explore the potential applications of our designed electrodes, one type of flexible asymmetric supercapacitors has been assembled using a simple method as described in Experimental Section. The schematic illustration of the flexible asymmetric supercapacitor is shown in Fig 6(a). SSM/CNT@PPy@$MnO_2$ and SSM/active carbon (SSM/AC) electrodes are separated by a polymer separator and wrapped by two PET membranes, serving as positive and negative electrodes, respectively. The insets at the bottom of Fig. 6(a) show the prototype of our assembled capacitors, which exhibits high flexibility without destroying the structural integrity of the device. The effective volume of the devices is about 2 cm × 1 cm × 100 μm. In the asymmetric device, the charge balance is very important and should follow the relationship $Q^+ = Q^-$.[42] Fig. S4 present comparative CVs of CNT@PPy@$MnO_2$ and SSM/AC electrodes at scan rate of 20 mV/s, suggesting that the two prepared electrodes could meet the require for a asymmetric capacitor. Fig. S5 shows the CVs of the optimized asymmetric supercapacitor at different window potentials (from 1.0 to 2.0 V) at a constant scan rate of 50 mV $s^{-1}$. It can be seen that the optimized asymmetric supercapacitors show an ideal capacitive behavior with rectangular CVs, even at the window potential up to 2 V. Thus, the CVs at different scan rates shown in Fig. 6(b) were totally carried out at window potential of 2 V. The obtained CVs exhibit rectangular-like shapes without obvious redox peaks, indicating an ideal capacitive behavior, and their profiles show little distortion with the scan rates increasing, even at a high scan rate of 200 mV $s^{-1}$, indicating the desirable fast charge/discharge property for the potential applications in high power devices.

To further evaluate the performance of the asymmetric supercapacitor, the GCDs at different current densities were tested and shown in Fig. 6(c). From these GCDs, it can be seen that the potentials of charge/discharge lines are nearly proportional to the charge/discharge time. This linear shape indicates a rapid I-V response, a small ESR, and an ideal capacitive characteristics.[6] Moreover, using these GCDs, the power densities and energy densities of the assembled devices can be calculated. The thickness of the devices is roughly evaluated by the total thickness of two electrodes, two PET membraces and one separator, which is determined to be 210 μm (Fig. S7). From the Ragone plots shown in Fig. 6(d), the energy density of CNT@PPy@$MnO_2$//AC show the maximum value of 38.42 W h $kg^{-1}$ (2.24 mW h $cm^{-3}$) at power density of 100 W $kg^{-1}$ (5.83 mW $cm^{-3}$), and even maintains at a high value of 22.87 W h $kg^{-1}$ (1.33 mW h $cm^{-3}$) at power density of 10000 W $kg^{-1}$ (0.583 W $cm^{-3}$), showing an excellent energy retention of 59.52%, which is much higher than those reported in other

works.[20, 22, 43, 49] Here, for comparison, two types of symmetric supercapacitors were also assembled using CNT@PPy@$MnO_2$ and CNT@$MnO_2$ electrodes. As shown in the corresponding Ragone plots (Fig. 6d), it can be seen that the energy densities of symmetric supercapacitors are much lower than those of asymmetric ones, and that of CNT@PPy@$MnO_2$// CNT@PPy@$MnO_2$ is much higher than that of CNT@$MnO_2$//CNT@$MnO_2$. Their maximum energy densities are 9.34 and 3.32 W h $kg^{-1}$ (0.31 and 0.086 mW h $cm^{-3}$) at the power density of 100 W $kg^{-1}$ (6.67 and 2.62 mW $cm^{-3}$), while their energy densities maintain 5.56 (59.5%) and 2.5 W h $kg^{-1}$ (75.3%) at the power density of 5000 W $kg^{-1}$, respectively. From these comparisons, it can be found that the maximum energy densities of two symmetric supercapacitors have a big difference at low power density, which can be ascribed to the slow electron transport and ion diffusion induced by the small current density. In our case, the advantages of perfect CNT@PPy@$MnO_2$ core-shell structures might be critical to high energy density. To get a direct comparison and adequately demonstrate the advantages of CNT@PPy@$MnO_2$ core-shell structures for supercapacitors, we compare our results to the performances of supercapacitors reported in other work that listed in Table 1. [20, 22, 43-49] The comparison further suggests this type of perfect CNT@PPy@$MnO_2$ core-shell structures are useful for high energy density supercapacitors.

For practical applications, the stabilities of the constructed supercapacitors are very important. First, the cycling stabilities the assembled supercapacitors (symmetric and asymmetric) were tested at charge/discharge current density of 5 A $g^{-1}$. The retention related to the initial specific capacitance is given in Fig. 6(e). After 2000 cycles, the CNT@PPy@$MnO_2$//AC asymmetric supercapacitors show a retention rate of about 89.7%, and the CNT@PPy@$MnO_2$//CNT@PPy@$MnO_2$ and CNT@$MnO_2$//CNT@$MnO_2$ symmetric ones respectively of about 87.2% and 73.7%, respectively, suggesting a high potential for practical applications. Moreover, the CVs under bending of 0º and 180º shown in Fig. S6 demonstrate an excellent performance for the potential flexible applications. Then, we have tested the bending stability of our assembled CNT@PPy@$MnO_2$//CNT@PPy@$MnO_2$ devices at scan rate of 100 mV $s^{-1}$. Fig. 6(f) shows the capacitance retention ratio as a function of the bending cycle numbers. The retention rate remains about 64.74% after 200 bending cycles with 180º, suggesting a good bending stability for practical flexible applications.

## Conclusions

In summary, we have successfully designed and fabricated a type of CNT@$MnO_2$ perfect core-shell structures under assistance of PPy, and investigated the importance of PPy in constructing 3D hierarchical carbon nanotube@$MnO_2$ perfect core-shell nanostructures. Compared to the previous reported direct loading of $MnO_2$ on CNT materials, this PPy treatment is very useful to deposit $MnO_2$ uniformly on CNTs, forming a perfect charge transfer channels. And the deposited $MnO_2$ induced by PPy is in form of nanosheets, which can further increase the specific surface area, enhance the accessibility of the ions. Electrochemical tests indicate that the CNT@PPy@$MnO_2$ single electrodes exhibits a high specific capacitance of 529.3 F $g^{-1}$ at current density of 0.1 A $g^{-1}$, which is much higher than that of CNT@$MnO_2$ ones (322.9 F $g^{-1}$ at 0.1

**Table 1** Energy density retention of the assembled 3D nanostructure supercapacitors reported in literatures compared with our flexible supercapacitors

| Supercapacitors | Power density Range (W $kg^{-1}$) | Energy density Range (W h $kg^{-1}$) | Flexibility | Reference |
|---|---|---|---|---|
| CNF/CNT/$MnO_2$//CNF/CNT/$MnO_2$ | 100-10000 | 3.88-2.5 | YES | [20] |
| 3DG/CNT/$MnO_2$//3DG/AC | 170.5-22727.3 | 33.71-19.16 | YES | [22] |
| $MnO_2$ nanowire/graphene//graphene | 100-5000 | 30.4-7.0 | NO | [43] |
| $MnO_2$/CNT textile//reduced $MnO_2$/CNT textile | 9000-13000 | 17.5-4 | YES | [44] |
| $MnO_2$/CNT//AC | 600-2100 | 13.3-8.5 | NO | [45] |
| Carbon/$MnO_2$ DNTAs//C | 16000-50000 | 35-30 | NO | [46] |
| CNT@$MnO_2$//ZNC | 1600-16000 | 20.44-14.22 | NO | [47] |
| CNP/$MnO_2$ nanorod// CNP/$MnO_2$ nanorod | 14000-15000 | 4.8-1 | YES | [48] |
| GNR/$MnO_2$//GNR | 12100-25900 | 29.4-22.5 | NO | [49] |
| CNT@PPy@$MnO_2$//AC | 100-30000 | 38.42-11.11 | YES | Our work |
| CNT@PPy@$MnO_2$// CNT@PPy@$MnO_2$ | 100-5000 | 9.34-5.56 | YES | Our work |

A $g^{-1}$). EIS result comparison suggests that this great enhancement in specific capacitance should be due to the well –designed perfect core-shell structure of CNT@$MnO_2$ and the grown $MnO_2$ nanosheets. Moreover, the excellent cycling stability with 98.5% retention of the initial specific capacitance after 2000 cycles is much higher than that of CNT@$MnO_2$ electrodes. Meanwhile, our assembled asymmetric CNT@PPy@$MnO_2$//AC devices show a high energy density of 38.42 W h $kg^{-1}$ (2.24 mW h $cm^{-3}$) at power density of 100 W $kg^{-1}$ (5.83 mW $cm^{-3}$), and maintain 59.52% of the initial value at 10000 W $kg^{-1}$ (0.583 W $cm^{-3}$), showing a high rate capability. In addition, the assembled devices show high cycle stability (89.7% after 2000 cycles), and bending stability (64.74% after 200 bending cycles). These impressive results suggest that our designed 3D hierarchical CNT@$MnO_2$ perfect core-shell nanostructures in this work might give a new insight for the development of high energy density flexible energy storage devices.

## Acknowledgements

This research was financially supported by the National Natural Science Foundation of China (Grant Nos. 51202100, 11474135, and U1232121), and partially by the Fundamental Research Funds for the Central Universities (NO. lzujbky-2015-110).

## Notes and references

1. D. Pech, M. Brunet, H. Durou, P. Huang, V. Mochalin, Y. Gogotsi, P. L. Taberna and P. Simon, *Nat Nano*, 2010, **5**, 651-654.
2. X. Lang, A. Hirata, T. Fujita and M. Chen, *Nat Nano*, 2011, **6**, 232-236.
3. D. R. Rolison, J. W. Long, J. C. Lytle, A. E. Fischer, C. P. Rhodes, T. M. McEvoy, M. E. Bourg and A. M. Lubers, *Chem. Soc. Rev.*, 2009, **38**, 226-252.
4. K. Naoi, W. Naoi, S. Aoyagi, J.-i. Miyamoto and T. Kamino, *Accounts. Chem. Res.*, 2013, **46**, 1075-1083.
5. J. Liu, H. Xia, L. Lu and D. Xue, *J. Mater. Chem.*, 2010, **20**, 1506-1510.
6. Y. M. He, W. J. Chen, X. D. Li, Z. X. Zhang, J. C. Fu, C. H. Zhao and E. Q. Xie, *Acs Nano*, 2013, **7**, 174-182.
7. Y. Ma, W. Chen, P. Zhang, F. Teng, J. Zhou, X. Pan and E. Xie, *RSC Adv.*, 2014, **4**, 47609-47614.
8. P. Simon and Y. Gogotsi, *Nat Mater*, 2008, **7**, 845-854.
9. X. Xiao, T. Li, P. Yang, Y. Gao, H. Jin, W. Ni, W. Zhan, X. Zhang, Y. Cao, J. Zhong, et al., *ACS Nano*, 2012, **6**, 9200-9206.
10. Y. Gao, H. Jin, Q. Lin, X. Li, M. M. Tavakoli, S.-F. Leung, W. M. Tang, L. Zhou, H. L. Wa Chan and Z. Fan, *J. Mater. Chem. A*, 2015, **3**, 10199-10204.
11. Q. Cheng, J. Tang, J. Ma, H. Zhang, N. Shinya and L.-C. Qin, *Carbon*, 2011, **49**, 2917-2925.
12. Y. M. He, W. J. Chen, C. T. Gao, J. Y. Zhou, X. D. Li and E. Q. Xie, *Nanoscale*, 2013, **5**, 8799-8820.
13. H. Jiang, P. S. Lee and C. Li, *Energy & Environmental Science*, 2013, **6**, 41-53.
14. C. Gong, Y. He, J. Zhou, W. Chen, W. Han, Z. Zhang, P. Zhang, X. Pan, Z. Wang and E. Xie, *Acs Appl. Mater. Interfaces*, 2014, **6**, 14844-14850.
15. Y. Hou, Y. Cheng, T. Hobson and J. Liu, *Nano Lett.*, 2010, **10**, 2727-2733.
16. Y. Cheng, S. Lu, H. Zhang, C. V. Varanasi and J. Liu, *Nano Lett.*, 2012, **12**, 4206-4211.
17. H. Xia, Y. Wang, J. Lin and L. Lu, *Nanoscale Research Letters*, 2012, **7**, 1-10.
18. Q. Li, X.-F. Lu, H. Xu, Y.-X. Tong and G.-R. Li, *ACS Appl. Mater. Interface*, 2014, **6**, 2726-2733.
19. Y. Qiu, G. Li, Y. Hou, Z. Pan, H. Li, W. Li, M. Liu, F. Ye, X. Yang and Y. Zhang, *Chemistry of Materials*, 2015, **27**, 1194-1200.
20. T. Wang, D. Song, H. Zhao, J. Chen, C. Zhao, L. Chen, W. Chen, J. Zhou and E. Xie, *J. Power Sources*, 2015, **274**, 709-717.
21. Q. Li, J. M. Anderson, Y. Chen and L. Zhai, *Electrochim. Acta*, 2012, **59**, 548-557.
22. W. J. Chen, Y. M. He, X. D. Li, J. Y. Zhou, Z. X. Zhang, C. H. Zhao, C. S. Gong, S. K. Li, X. J. Pan and E. Q. Xie, *Nanoscale*, 2013, **5**, 11733-11741.
23. M. Zhi, C. Xiang, J. Li, M. Li and N. Wu, *Nanoscale*, 2013, **5**, 72-88.
24. H. Huang, W. Zhang, Y. Fu and X. Wang, *Electrochim. Acta*, 2015, **152**, 480-488.
25. M. C. Tu, H. Y. Chen, Y. Wang, S. M. Moochhala, P. Alagappan and B. Liedberg, *Anal. Chim. Acta*, 2015, **853**, 228-233.
26. P. Li, Y. Yang, E. Shi, Q. Shen, Y. Shang, S. Wu, J. Wei, K. Wang, H. Zhu, Q. Yuan, et al., *Acs Appl. Mater. Interfaces*, 2014, **6**, 5228-5234.
27. N. Sano, Y. Hori, S. Yamamoto and H. Tamon, *Carbon*, 2012, **50**, 115-122.
28. J. Tao, N. Liu, W. Ma, L. Ding, L. Li, J. Su and Y. Gao, *Sci Rep*, 2013, **3**, 2286.
29. W. Chen, Y. He, X. Li, J. Zhou, Z. Zhang, C. Zhao, C. Gong, S. Li, X. Pan and E. Xie, *Nanoscale*, 2013, **5**, 11733-11741.
30. H. R. Ghenaatian, M. F. Mousavi and M. S. Rahmanifar, *Electrochim. Acta*, 2012, **78**, 212-222.
31. J. Tao, N. Liu, W. Ma, L. Ding, L. Li, J. Su and Y. Gao, *Sci. Rep.*, 2013, **3**, 1-7.
32. X. Xie and L. Gao, *Carbon*, 2007, **45**, 2365-2373.
33. J. Zhou, G. Sun, Z. Zhan, J. An, L. Zheng and E. Xie, *Appl. Phys. Lett.*, 2013, **103**, 031912.
34. A. Ogata, S. Komaba, R. Baddour-Hadjean, J. P. Pereira-Ramos and N. Kumagai, *Electrochim. Acta*, 2008, **53**, 3084-3093.
35. H. Xia, M. Lai and L. Lu, *J. Mater. Chem.*, 2010, **20**, 6896.
36. S. Schantz, L. M. Torell and J. R. Stevens, *J. Appl. Phys.*, 1988, **64**, 2038.
37. Y. C. Liu and B. J. Hwang, *Thin Solid Films*, 1999, **339**, 233-239.
38. J. Duchet, R. Legras and S. Demoustier-Champagne, *Synthetic. Met.*, 1998, **98**, 113-122.
39. S. Bose, T. Kuila, A. K. Mishra, R. Rajasekar, N. H. Kim and J. H. Lee, *J. Mater. Chem.*, 2012, **22**, 767-784.

40. X. Li, X. Zang, Z. Li, X. Li, P. Li, P. Sun, X. Lee, R. Zhang, Z. Huang, K. Wang, et al., *Adv. Funct. Mater.*, 2013, **23**, 4862-4869.
41. C. Kim and K. S. Yang, *Appl. Phys. Lett.*, 2003, **83**, 1216-1218.
42. Z. Fan, J. Yan, T. Wei, L. Zhi, G. Ning, T. Li and F. Wei, *Adv. Funct. Mater.*, 2011, **21**, 2366-2375.
43. Z.-S. Wu, W. Ren, D.-W. Wang, F. Li, B. Liu and H.-M. Cheng, *ACS Nano*, 2010, **4**, 5835-5842.
44. L. Hu, W. Chen, X. Xie, N. Liu, Y. Yang, H. Wu, Y. Yao, M. Pasta, H. N. Alshareef and Y. Cui, *ACS Nano*, 2011, **5**, 8904-8913.
45. L. Li, Z. A. Hu, N. An, Y. Y. Yang, Z. M. Li and H. Y. Wu, *The Journal of Physical Chemistry C*, 2014, **118**, 22865-22872.
46. Q. Li, X. F. Lu, H. Xu, Y. X. Tong and G. R. Li, *Acs Appl. Mater. Interfaces*, 2014, **6**, 2726-2733.
47. R. R. Salunkhe, H. Ahn, J. H. Kim and Y. Yamauchi, *Nanotechnology*, 2015, **26**, 204004.
48. L. Yuan, X.-H. Lu, X. Xiao, T. Zhai, J. Dai, F. Zhang, B. Hu, X. Wang, L. Gong, J. Chen, et al., *ACS Nano*, 2012, **6**, 656-661.
49. M. Liu, W. W. Tjiu, J. Pan, C. Zhang, W. Gao and T. Liu, *Nanoscale*, 2014, **6**, 4233-4242.